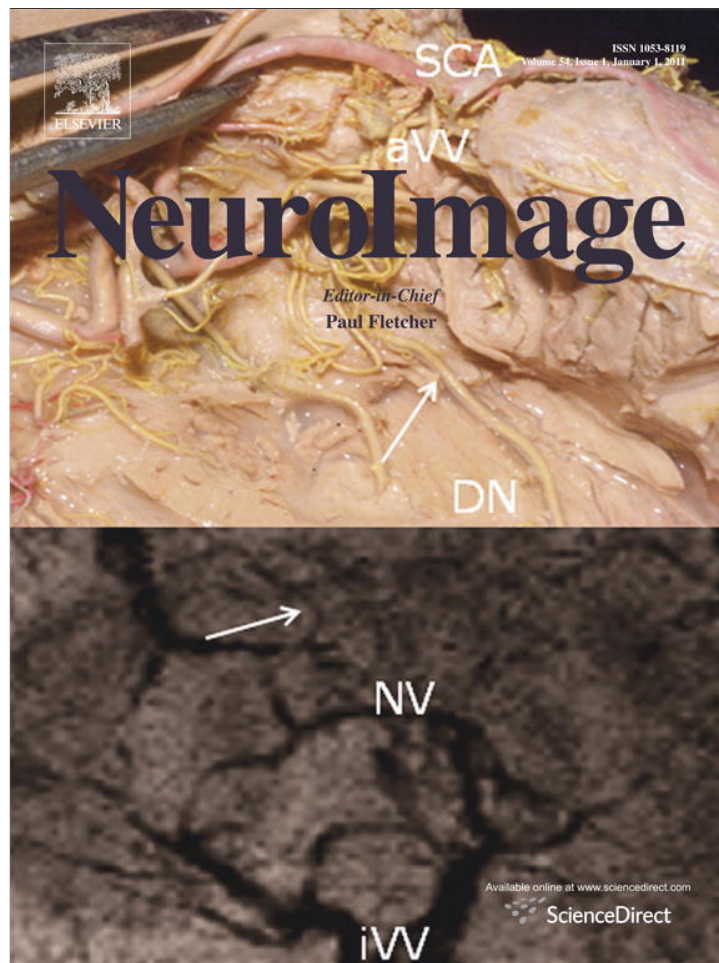


Provided for non-commercial research and education use.
Not for reproduction, distribution or commercial use.



(This is a sample cover image for this issue. The actual cover is not yet available at this time.)

This article appeared in a journal published by Elsevier. The attached copy is furnished to the author for internal non-commercial research and education use, including for instruction at the authors institution and sharing with colleagues.

Other uses, including reproduction and distribution, or selling or licensing copies, or posting to personal, institutional or third party websites are prohibited.

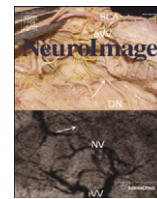
In most cases authors are permitted to post their version of the article (e.g. in Word or Tex form) to their personal website or institutional repository. Authors requiring further information regarding Elsevier's archiving and manuscript policies are encouraged to visit:

<http://www.elsevier.com/copyright>



Contents lists available at SciVerse ScienceDirect

NeuroImage

journal homepage: www.elsevier.com/locate/ynimg

Full Length Articles

Biochemical label-free tissue imaging with subcellular-resolution synchrotron FTIR with focal plane array detector

M.Z. Kastyak-Ibrahim^a, M.J. Nasse^{b,c}, M. Rak^b, C. Hirschmugl^b, M.R. Del Bigio^d,
B.C. Albensi^e, K.M. Gough^{a,*}

^a Department of Chemistry, University of Manitoba, Winnipeg, Manitoba, Canada R3T 2N2

^b Department of Physics, University of Wisconsin-Milwaukee, Milwaukee, WI 53211, USA

^c Synchrotron Radiation Center, University of Wisconsin-Madison, Stoughton, WI 53589, USA

^d Department of Pathology, University of Manitoba, Winnipeg, Manitoba, Canada R3E 0W3

^e Department of Pharmacology and Therapeutics, Faculty of Medicine, University of Manitoba, and Principal Investigator, Division of Neurodegenerative Disorders, St. Boniface Hospital Research Centre, Winnipeg, Manitoba, Canada R3E 0W3

ARTICLE INFO

Article history:

Received 1 May 2011

Revised 18 November 2011

Accepted 23 November 2011

Available online 16 December 2011

Keywords:

Neuron

Brain

Alzheimer

Retina

FTIR imaging

IRENI

ABSTRACT

The critical questions into the cause of neural degeneration, in Alzheimer disease and other neurodegenerative disorders, are closely related to the question of why certain neurons survive. Answers require detailed understanding of biochemical changes in single cells. Fourier transform infrared microspectroscopy is an excellent tool for biomolecular imaging *in situ*, but resolution is limited. The mid-infrared beamline IRENI (InfraRed ENvironmental Imaging) at the Synchrotron Radiation Center, University of Wisconsin-Madison, enables label-free subcellular imaging and biochemical analysis of neurons with an increase of two orders of magnitude in pixel spacing over current systems. With IRENI's capabilities, it is now possible to study changes in individual neurons *in situ*, and to characterize their surroundings, using only the biochemical signatures of naturally-occurring components in unstained, unfixed tissue. We present examples of analyses of brain from two transgenic mouse models of Alzheimer disease (TgCRND8 and 3xTg) that exhibit different features of pathogenesis. Data processing on spectral features for nuclei reveals individual hippocampal neurons, and neurons located in the proximity of amyloid plaque in TgCRND8 mouse. Elevated lipids are detected surrounding and, for the first time, within the dense core of amyloid plaques, offering support for inflammatory and aggregation roles. Analysis of saturated and unsaturated fatty acid ester content in retina allows characterization of neuronal layers. IRENI images also reveal spatially-resolved data with unprecedented clarity and distinct spectral variation, from sub-regions including photoreceptors, neuronal cell bodies and synapses in sections of mouse retina. Biochemical composition of retinal layers can be used to study changes related to disease processes and dietary modification.

© 2011 Elsevier Inc. All rights reserved.

Introduction

The ability to visualize neurons in central nervous system (CNS) tissue is a fundamental requirement in neuroscience. Traditional post-mortem tissue analyses include a multitude of histochemical and immunohistochemical stains, designed to reveal specific molecules, aggregates or cells. Though well-developed and powerful, staining techniques for detection of specific chemical components are mostly non-quantitative, often only relatively specific, and somewhat unpredictable. The

Abbreviations: A β , amyloid beta; AD, Alzheimer disease; APP, amyloid protein precursor; CA, cornu ammonis; CH₂, methylene group; CNS, central nervous system; DG, dentate gyrus; DHA, docosahexaenoic acid; FPA, focal plane array; FTIR, Fourier transform infrared spectroscopy; IRENI, InfraRed ENvironmental Imaging; PUFA, polyunsaturated fatty acids; satFA, saturated fatty acids; SRC, Synchrotron Radiation Center.

* Corresponding author at: Department of Chemistry, Room 360 Parker Building, University of Manitoba, Winnipeg, Manitoba, Canada R3T 2N2. Fax: +1 204 474 7608.

E-mail address: kmgough@cc.umanitoba.ca (K.M. Gough).

chemistry of binding in some cases is understood well, but in others, remains unknown. The use of fluorescent dyes may be problematic: they can be cytotoxic for *in vivo* imaging, and may interact with critical cellular components, or interfere with drug action.

Many new physical imaging methods are being developed to visualize single cells, from two-color *in vivo* imaging with fluorescent proteins, e.g.: imaging photoreceptors with "Tomato/GFP-FLP/FRT" (Gambis et al., 2011), through non-destructive three-dimensional X-ray imaging with computed microtomography (Schulz et al., 2010) or SAXS-CT (Jensen et al., 2011), to third-harmonic generation (THG) microscopy for label-free brain imaging *in vivo* (Witte et al., 2011). Advances in Magnetic Resonance Imaging (MRI) are leading to smaller voxels, and the instrumentation is in widespread clinical practice. Each method is directed towards specific goals and, while results are impressive, all methods have both strengths and limitations. Genetic incorporation of fluorescent proteins labels only proteins. Spatially resolved SAXS or SAXS-CT enables the identification of nanometer-size features with periodicity that can

be attributed to the lamellar structure of myelin sheaths (Jensen et al., 2011). Detection of Purkinje cells in the cerebellum, by means of grating-based X-ray microtomography with phase contrast and without staining, has been reported (Schulz et al., 2010); however, just as with the SAXS-CT, the 3D image contains morphological but not direct spectrochemical information. THG spatial resolution is comparable to average neuronal cell size and the biochemical information obtained with THG imaging is limited. MRI voxels are much larger than individual neurons. A combined approach of multi-modal imaging, wherein many of these different, complementary techniques are employed, is proving to be the most successful means of advancing our knowledge.

Fourier transform infrared (FTIR) microspectroscopy provides label-free, molecular-specific images that show the distribution of myriad components in tissue sections (Seshadri et al., 1999; Chalmers and Griffiths, 2002); hence it represents a powerful, complementary technique to standard and novel tissue analyses. A key aspect is that characteristic infrared absorption peaks from all tissue components (e.g.: proteins, lipids, carbohydrates, and nucleic acids) are detected simultaneously at each pixel, *in situ*, without staining. Relevant factors for successful spectral analysis include physical size, tissue heterogeneity, degree to which macromolecules differ from each other (chemical composition, molecular conformation) and presence of spectrally resolvable, distinguishing marker peaks. While FTIR is an increasingly valuable tool for surveying tissue, the capability to analyze tissue sections at the subcellular level is requisite to advance this field.

The quality of FTIR images depends on the quality of the sample and on the spatial resolution of the instrument. In an ideal far-field system, the best achievable spatial resolution is fundamentally determined by diffraction and is thus wavelength-dependent. The spatial resolution of dual-aperture/confocal-type IR microscopes equipped with a single element detector is determined by the aperture size (Carr, 2001). Standard IR instruments employ a thermal light source that cannot be collimated efficiently, incurring large photon loss at the detector. To increase spatial resolution, aperture size is decreased, leading to deteriorating signal-to-noise that must be compensated by significantly longer acquisition times. The much higher brightness of a synchrotron source allows apertures down to $\sim 5 \times 5 \mu\text{m}^2$, while keeping acquisition times reasonable. In the best case, aperture size (spatial resolution) is limited to $\sim 15 \times 15 \mu\text{m}^2$ for thermal source instruments and $\sim 3 \times 3 \mu\text{m}^2$, at the shorter wavelengths, for conventional synchrotron-based systems (Dumas et al., 2007).

Apertureless, wide-field imaging systems equipped with a focal plane array (FPA), a multi-element detector with up to 128×128 pixels in a single tile, are becoming common (Huffman et al., 2002). Larger images are constructed as seamless mosaics of individual tiles. In comparison to our early work with synchrotron confocal, single pixel microscopy, we can now obtain data of comparable quality from a thermal source, ~ 100 times faster, with our Varian 670 FTIR and 620 microscope equipped with a 64×64 pixel FPA (U. Manitoba). Despite the gains in speed and simplicity, spatial resolution is no better. In this case, the magnification is $7.5\times$, and the effective geometric pixel size is $5.5 \times 5.5 \mu\text{m}^2$. The image is spatially under-sampled because the effective sample pixels are too large to yield diffraction-limited images for smaller wavelengths, and are increasingly blurred due to diffraction of light across multiple pixels at longer wavelengths (Nasse et al., 2011; Miller and Smith, 2005). This problem is now resolved with the synchrotron-source FTIR-FPA system IRENI.

The mid-infrared beamline IRENI, at the Synchrotron Radiation Center (SRC), University of Wisconsin at Madison, is the first synchrotron-based wide-field IR imaging system, uniquely combining 12 synchrotron beams to homogeneously illuminate a large area of the sample (Nasse et al., 2007, 2011). Here, a $74\times$ objective is used to image the transmitted light onto a 128×128 FPA; more homogeneous S/N can be obtained over the imaging area by selecting a smaller tile size. Biochemical images are obtained with an effective pixel size of $0.54 \times 0.54 \mu\text{m}^2$, the highest far-field spatial sampling currently

achievable. Oversampling enables the highest spatial resolution at all wavelengths in the mid-IR bandwidth, as demonstrated with a calibrated standard Air Force Target. The images are diffraction-limited even at the shortest mid-IR wavelengths ($2.5 \mu\text{m}$); acquisition time is $\sim 10^4$ faster than could be achieved with the same system and a thermal source (Nasse et al., 2011).

We present subcellular images of brain sections from two mouse models for Alzheimer disease (AD) and retina from a wild type mouse to illustrate the discoveries enabled by IRENI. Data analyses include spectrochemical subcellular imaging and biochemical analysis of neurons in the hippocampus from a 3xTg mouse, dense core amyloid plaques and surrounding neurons in the cortex of a TgCRND8 mouse, and neurons in retina sections, where imaging data are relevant for age-related macular degeneration, oxidative stress and neurodegeneration.

Materials and methods

Mouse tissue sections

Brain samples were acquired from two different mouse models of AD: TgCRND8 and 3xTg and retina from a wild type mouse (C57BL/6) that is the background for the 3xTg strain. TgCRND8 expresses two familial AD mutations, the Swedish K670N/M671L and Indiana V717F variants in the human amyloid protein precursor (APP). The triply mutant mouse model, 3xTg, carries the K670N/M671L mutation in APP, the presenilin mutation PS1 (M146V) and the human four-repeat Tau harboring the P301L mutation (Oddo et al., 2003).

Mice are killed by decapitation under isoflurane anesthesia. All experimental protocols for animal studies were approved by appointed Protocol Management Review committees at the University of Toronto and University of Manitoba, following guidelines established by the Canadian Council for Animal Care. Details of sample acquisition for TgCRND8 are previously described in Kuzyk et al. (2010); the same protocol has been followed for animals from 3xTg mice (housed at the St. Boniface Research Centre, Winnipeg, Manitoba), with the exception of the freezing process. For the latter, brains and eyes were frozen by coating the fresh tissue with optimal cutting temperature compound (Sakura Finetek Inc. USA), and immersing in isopentane cooled in liquid nitrogen. Cryomicrotome sections ($6\text{--}8 \mu\text{m}$ thickness) were mounted onto appropriate substrates, either BaF₂ windows for transmission, or MirrIR (Kevley Technologies, Chesterland, OH, USA) for transfection. The tissue sections were dried in air, in the dark, in a dust free environment.

Amyloid beta 1–42 for FTIR reference spectrum of β -sheet protein

The synthetic amyloid β -protein fragment 1–42 (A β 42) (Sigma Chemical Co., St. Louis, MO, USA) was dissolved in phosphate buffer (pH = 7.6) at $\sim 1.25 \text{ mg mL}^{-1}$. The solution was filtered through a sterile Anotop-10 syringe filter incorporating an aluminum oxide membrane, $0.02 \mu\text{m}$ pore, to exclude pre-formed aggregates. Dilute samples of A β 42 were incubated at 37°C for up to 30 days. Samples for IR analysis were prepared by placing $5 \mu\text{L}$ aliquots from 60 to $70 \mu\text{M}$ peptide solution (or suspension) on a reflective MirrIR slide and drying under vacuum for $15\text{--}20$ minutes. Aggregation status was confirmed by TEM of a $2 \mu\text{L}$ aliquot from the same solution, mounted on a standard TEM grid (data not shown).

FTIR data collection

Spectra were acquired in transmittance or transreflectance mode at 4 cm^{-1} spectral resolution, from 4000 to 900 cm^{-1} , with Happ–Genzel apodization. Typically, 128 interferograms were co-added and ratioed to a similar background scan recorded at a blank region of the substrate.

Larger spatial pixelation, therefore lower resolution, thermal source FTIR-FPA survey images were first collected on a Varian 670-IR FTIR spectrometer equipped with a Varian 620-IR Imaging Microscope (University of Manitoba). FTIR-FPA images were acquired in transmission using a 64×64 pixel array, effective geometric pixel size $5.5 \times 5.5 \mu\text{m}^2$. Spectral analysis was performed with Resolutions Pro software (Version 5.0.0.700, Varian) or with routines run under MATLAB®, 2009. A reference spectrum of aggregated, pure A β 42 mounted on MirrIR was recorded in transmittance mode using a Nicolet Nexus 870 (University of Manitoba, Canada). The spectrum was acquired using a $1.5 \times 3 \text{mm}^2$ aperture and coaddition of 256 scans.

High resolution, synchrotron source FTIR (sFTIR) image data were recorded in transmission with IRENI at SRC, University of Wisconsin-Madison. sFTIR images were acquired using a $74 \times$ objective (Ealing Inc., Rocklin, CA, USA), yielding an effective geometric pixel size of $0.54 \times 0.54 \mu\text{m}^2$ at the sample plane; 128 scans were co-added. Images were analyzed with OPUS software (Version 6.0, Bruker).

FTIR spectral analysis

Lipid distribution was shown by differences in the intensities of the symmetric CH₂ band envelope (peak: 2850cm^{-1} , area under curve from 2862 to 2842cm^{-1}) and the lipid carbonyl (peak: 1735cm^{-1} , area under curve between 1750 and 1724cm^{-1}). Dense core plaque was identified from the area of the β -sheet amide I shoulder (peak: 1630cm^{-1} , area under curve between 1640 and 1620cm^{-1}) or a newly-discovered band with maximum at 1390cm^{-1} (area under curve between 1415 and 1370cm^{-1}). Additional bands used for the processing of retina spectral data include a peak characteristic for polyunsaturated fatty acid esters (3010cm^{-1} , area under curve between 3026 and 3000cm^{-1}), a peak attributed to nucleic acids (1712cm^{-1} , area under curve between 1725 and 1700cm^{-1}) and a peak characteristic for collagen (1204cm^{-1} , area under curve between 1214 and 1197cm^{-1} ; Wiens et al., 2007). For each case, the linear baseline was set at the same limits as the band envelope. Spectra presented in figures were extracted individually from images collected with the IRENI system.

Hematoxylin stain

In order to help identify tissue morphology, a serial section of retina and the IR-imaged mouse brain tissue on barium fluoride (following IR analysis) were stained with the nuclear dye hematoxylin. The sections were fixed for 2 minutes in ethanol, rinsed in water, and placed in Mayer's hematoxylin (Sigma) for 5 minutes. They were then rinsed in tap water, dehydrated and coverslipped with Permount (Fisher).

Results and discussion

Biochemical changes occurring in neurodegenerative disorders affect neurons; however, not all neurons are affected in the same way or to the same degree. IRENI makes it possible to seek and study chemical changes in single cells. The new opportunities enabled by the IRENI imaging system present new challenges: since no comparable spectrochemical images, i.e., subcellular spatial resolution, have been obtained before, variations in individual spectra must now be reinterpreted in order to assign details to specific organelles. We have been using several imaging techniques to study AD, a progressive neurodegenerative disorder characterized by memory loss, dementia, amyloid plaques and tangles. The pathogenesis of AD remains unclear; however progress is being made in our understanding and in potential treatments to control or delay onset (Schjeide et al., 2009; Lucas et al., 2006; Mattson, 2004; Selkoe, 2004). Here, we have analyzed FTIR images of tissue from two animal models for

AD: hippocampal (cornu ammonis—CA1 subfield) pyramidal neurons in 3xTg mouse and neurons in the proximity of an amyloid beta (A β) plaque in TgCRND8 mouse, as well as in retina from a control mouse, C57BL/6, which is the background for the 3xTg model. Impaired retinal function is observed in numerous neurodegenerative diseases, including AD (Guo et al., 2010); detailed imaging is also critical for studies in age-related macular degeneration (Kokotas et al., 2011).

CA1 neurons in mouse hippocampal tissue

In the TgCRND8 mouse model, characteristic A β plaques are seen as early as 4 months (Chishti et al., 2001). In the 3xTg mouse, elevated APP is reported intraneuronally in the neocortex (3 months), then in hippocampal CA1 pyramidal neurons; and extraneuronally by 6 months in neocortex; plaques do not develop until many months later (Oddo et al., 2003; Winton et al., 2011). In the 3xTg model, aggregated plaques develop more slowly than in the TgCRND8 model, along with late onset formation of neurofibrillary tangles from hyperphosphorylated tau protein.

A photomicrograph of hippocampus from a 10-month-old 3xTg mouse, containing neurons of CA1 and dentate gyrus (DG), is shown in Fig. 1A. Contrast in the unfixed, frozen tissue section derives from differential density of tissue components. The corresponding Varian 670/620 FPA-FTIR data cube was processed on the area of the symmetric CH₂ stretch band envelope, peak at 2850cm^{-1} , to create images of the lipid distribution (Fig. 1B). Results of this processing for lipid are presented as a spectrochemical false-color image wherein pixels have been blended to facilitate appreciation of morphology. The distinctive colors corresponding to different morphology in the brain tissue arise from the naturally-occurring variation in lipid

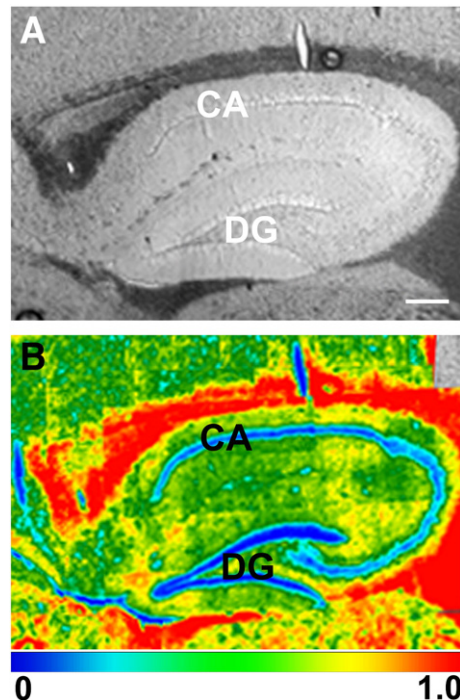


Fig. 1. FTIR-FPA imaging of 3xTg mouse hippocampal tissue with a thermal source FPA-FTIR microscope shows tissue morphology. A) Photomicrograph of a brain section from the hippocampus region. B) FTIR image processed for lipid carbonyl band, 1738cm^{-1} . Varian ResPro software aggregates pixels in large mosaics: tiles reduced from 64×64 to 32×32 pixels and blended. Color bar indicates lipid gradient from low (blue, C=O band area <0.0) to high (red, C=O band area >1.0). The regions with concentrated neuronal nuclei in the dentate gyrus (DG) and cornu ammonis (CA) are blue because there is negligible lipid in nuclei. The alveus dorsal to (above) the cornu ammonis is red because it has high myelin content. Scale bar = $100 \mu\text{m}$.

content of each component of the tissue. Regions of highest lipid membrane content, such as white matter of the alveus, appear as red; gray matter with lower lipid content is shown as green/yellow. The CA and DG are characterized by densely packed neuron bodies that are much less abundant in lipid membranes; these appear as blue arcs across the hippocampus. The general outline of the CA neurons is clearly defined; however, individual neuronal bodies cannot be distinguished.

This simple test for relative lipid distribution reveals tissue morphology, yielding results that are comparable with those from stains (Kastyak et al., 2010). FPA-FTIR imaging with the thermal source spectrometer thus offers the potential to monitor overall changes in tissues through rapid data collection across large areas of tissue, e.g. 1 cm² in a few hours. Data collected with a thermal source FTIR imaging instrument facilitates identification of the most important regions for subsequent imaging on the IRENI system at SRC.

A photomicrograph of CA1 region in a desiccated tissue section from 10-month-old 3xTg mouse hippocampus, mounted on a BaF₂ window, is shown in Fig. 2A. The tissue was stained with hematoxylin to show the location of nuclei, following acquisition of the FTIR images with the thermal source and with IRENI. The CA1 band is actually about 3–5 neuron cell bodies deep; the nuclei of CA1 pyramidal neurons are stained deeper blue in the photomicrograph. Pale lines reveal hairline cracks in this tissue, artifacts from desiccation and freezing.

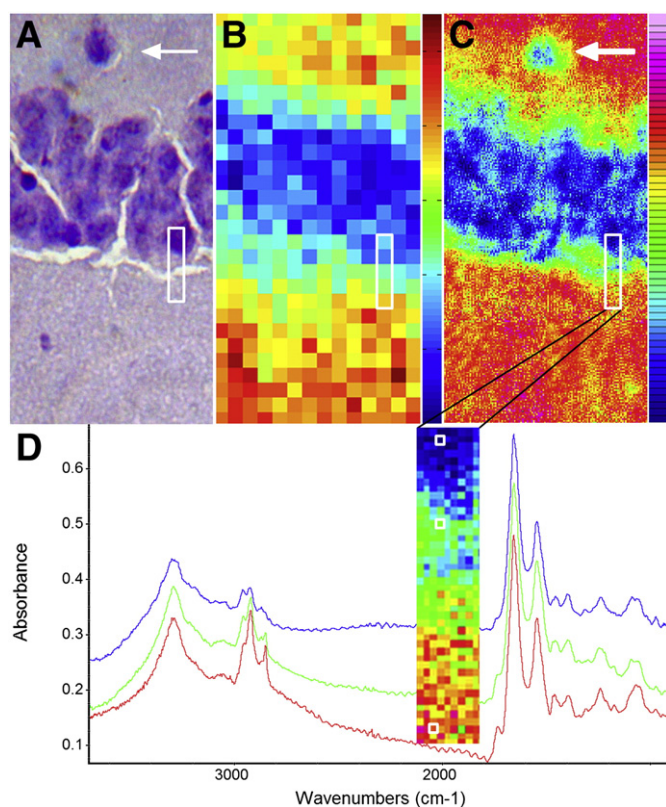


Fig. 2. FTIR-FPA images of 3xTg mouse hippocampal tissue with IRENI system, processed for lipid, reveals subcellular resolution of neuron composition. A) Photomicrograph of pyramidal neurons in cornu ammonis; nuclei stained with hematoxylin. B) FTIR-FPA image collected with a thermal source and processed with MATLAB®, 2009 for true pixel display, and C) with IRENI. White box (~5.5 × 27.5 μm) in (A) includes a nucleus, cytoplasm and neuropil; box corresponds to 5 pixels in (B), and 500 pixels in (C). D) White boxed area in (C) is enlarged 5 fold to show raw IRENI pixels. Spectra from three pixels (white outline in insert, normalized to amide I peak height and offset for clarity) show differences between the nuclear (blue), cytoplasmic (green), and white matter (red) regions. Color bar for thermal source image is as in Fig. 1; for IRENI, range is from 0 to 0.75. (For interpretation of the references to color in this figure legend, the reader is referred to the web version of this article.)

Simply processing images on the area of the CH₂ symmetric stretch band is sufficient to reveal the location of the cell bodies. The CA1 band is 3 to 5 neuron cell bodies deep, but only their general location can be seen in the thermal source FTIR image (Fig. 2B). The false-color IR spectrochemical image is displayed as unblended pixels, after processing in MATLAB®, 2009. A block of ~14 × 28 (392) pixels in the thermal source image corresponds to the entire area imaged with IRENI, where the effective geometric pixel size of 0.54 × 0.54 μm² results in a mosaic of 128 × 256 (32,768) pixels (Fig. 2C). An isolated cell body, visible in the stained tissue (white arrow, Fig. 2A), is not detected by the thermal source (Fig. 2B), but is easily detected by IRENI (white arrow, Fig. 2C).

Information-rich spectra obtained with IRENI are illustrated in Fig. 2D, where a block of ~500 pixels, corresponding to 5 pixels in the Varian image, is expanded to show the individual pixels, along with three spectra taken from spectrochemically distinct points. The top spectrum in Fig. 2D, from a pixel in the darkest blue region of a cell interior, has the least lipid content, and corresponds to a nucleus (Fig. 2A). Increasing sub-cellular lipid due to organelle membranes within the cell is seen in the middle spectrum. Lipid is significantly increased in the neuropil (bottom spectrum).

Spectral information obtained with IRENI offers the possibility of a significantly more detailed analysis of individual cells. The 3xTg mouse first develops abnormal amounts of amyloid protein precursor within neurons, only showing increased amounts of extracellular Aβ 40 and Aβ 42 peptides by 12 months (Oddo et al., 2003). Very recently (Winton et al., 2011), application of a suite of stains has shown that it is only the full-length APP that is elevated in the neurons of the young 3xTg mice, where it is accumulated increasingly in the cell body. The breakdown of APP into the plaque-forming peptides does not begin until 10 to 12 months of age. 4G8 staining of a serial section of this 10-month 3xTg mouse was positive (APP or Aβ), but Congo red stain for β-sheet did not reveal any aggregated amyloid (data not shown). The absence of a β-sheet signature in the IR spectra of the neurons is consistent with the absence of plaque-forming peptides at this age. IRENI imaging will enable us to monitor neuronal changes as the disease progresses. While the lipid content remains relatively similar through spectra 3–5, other differences in the fingerprint region are immediately obvious from a cursory comparison of the spectra. Other differences between spectra must correspond to different sub-cellular components, but more comprehensive, multidimensional analyses will be required to mine the data now becoming available.

Alzheimer-type plaques

FTIR spectra reveal plaques and evidence of inflammation, including elevated lipid that surrounds dense-core plaques and may permeate the diffuse, non-aggregated periphery (Rak et al., 2007; Kuzyk et al., 2010). The latter data were obtained from plaques in the TgCRND8 mouse model using a conventional, single pixel raster-scan synchrotron-based FTIR system or a thermal source FPA-FTIR microscope. The results obtained with IRENI on tissue from the same animal model reveal spectroscopic details accessible only with the higher spatial resolution.

The photomicrographs and processed FTIR image data from the same plaque and adjacent tissue in the cortex of a 15-month-old TgCRND8 mouse, collected with the Varian thermal source FPA-FTIR instrument and the IRENI system, are shown in Fig. 3A–D and E–F, respectively. Both FTIR images have been processed on lipid distribution (2850 cm⁻¹ peak; Fig. 3B and F) to show morphology, regions containing abnormal amounts of β-sheet protein (1630 cm⁻¹ peak; Fig. 3C and G), and plaque core (1390 cm⁻¹ peak; Fig. 3D and H). IRENI spectra, extracted from specific features of interest, and the spectrum of pure aggregated Aβ are shown in Fig. 3I.

The spectrum of aggregated Aβ42 shows the characteristic strong amide I band with a maximum at 1630 cm⁻¹, a moderate amide I

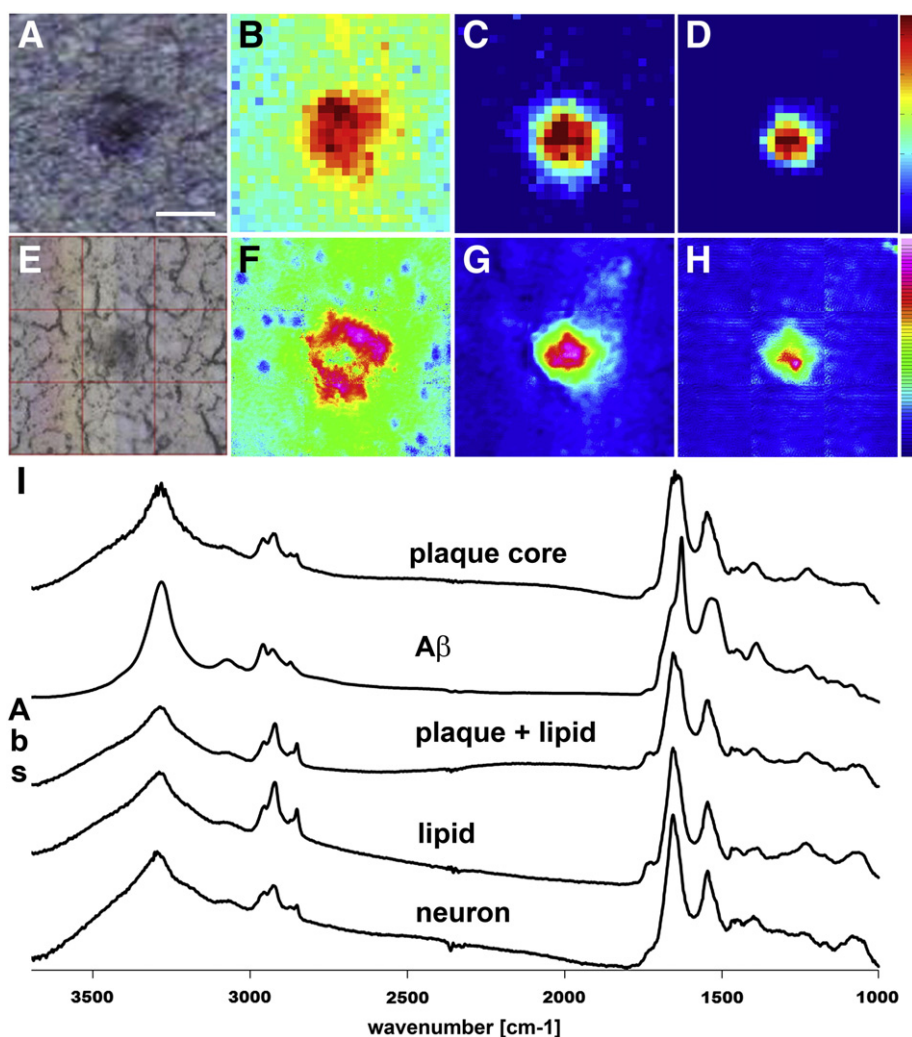


Fig. 3. FTIR images of an Alzheimer type neuritic plaque in TgCRND8 mouse cortex. (A and E) Photomicrographs of plaque and adjacent tissue. (B–D) Thermal source FPA-FTIR images processed with MATLAB®, 2009 to permit true pixel representation and (F–H) pixelated IRENI images. FTIR spectrochemical images are processed to show (B and F: 2850 cm^{-1}) lipid distribution in plaque and adjacent tissue; (C and G: 1630 cm^{-1}) aggregated β -amyloid protein; (D and H: 1390 cm^{-1}) densest region of plaque core. I) IRENI spectra extracted from plaque dense core, surrounding lipid envelope, adjacent neuropil and neuron cell body, normalized to amide I (1655 cm^{-1}). A spectrum of pure A β 42 is shown below spectrum from plaque core. Color bars indicate gradient from low (blue) to high (red), based on integrated band areas: B) 2850 cm^{-1} , 0–0.7; C) 1630 cm^{-1} , 0.0–0.35; D) 1390 cm^{-1} , 0.4–1.0. Scale bar $30\text{ }\mu\text{m}$. (For interpretation of the references to color in this figure legend, the reader is referred to the web version of this article.)

shoulder at about 1650 cm^{-1} and a weaker shoulder at 1692 cm^{-1} . The amide II is broader than that for α -helical protein, and shifted to lower energy. There is also a noticeable band, maximum at $\sim 1390\text{ cm}^{-1}$, previously unreported for plaque; FTIR literature on the A β peptide has focused almost exclusively on the distinct amide I region. The assignment is not yet clear: it could include a methyl deformation mode, since one third of the residues carry a methyl group, as well as the carboxylate band, since both lie in this region; it might also be due to alteration of the peptide backbone into β -sheet conformation.

When the thermal source images are processed for lipid, cell bodies in the tissue surrounding the plaque are indistinguishable from the surrounding tissue, (Fig. 3B), but are immediately revealed as small ovoids (blue in the spectral rendering used here) in the IRENI image (Fig. 3F). A spectrum from the cell interior also shows spectral characteristics of DNA (1712 cm^{-1}), now more apparent in the absence of lipid carbonyl at 1738 cm^{-1} , as well as differences in the fingerprint region. The spectra of the nearby cell bodies are free of amyloid signature or other anomalies, indicating that they are as yet unaffected by this dense core plaque. In the thermal-source image (Fig. 3B), lipid dominates the central portion of the tile, surrounding

and overlaying the plaque. In the IRENI image (Fig. 3F), the intensity of the lipid peak reaches its maximum value outside the amyloid plaque core, marking the lipid envelope that surrounds the plaque and decreases gradually into adjacent tissue.

The amyloid plaque is readily visualized by processing on the intensity at 1630 cm^{-1} , in both maps (Fig. 3 C,G); however, the IRENI image now provides additional insight into the plaque composition. The plaque core is often too dense to produce a good quality amide I band but, using the band at 1390 cm^{-1} , we can isolate the region of most concentrated β -sheet content, visible as the dense core (Fig. 3 D,H).

The existence of a lipid envelope has been shown in our previous papers (Rak et al., 2007, Kuzyk et al., 2010). Significantly, the envelope coincides with regions that stained immunopositive for the A β peptide, but negative for β -sheet aggregation. The spectrum of plaque core is distinctly different from that of adjacent tissue but some lipid signature remains, proving that lipid permeates even the core. At the same time, we can now see that the β -sheet content is still detectable within the lipid envelope region (previously unresolved), as evidenced by the simultaneous elevation in CH₂ and the presence of the 1630 cm^{-1} shoulder in the spectrum labeled plaque + lipid (Fig. 3I).

Elevated lipid could indicate that the hydrophobic A β peptide is stabilized within a hydrophobic envelope; it could mean that the amyloid is actually being sequestered from surrounding tissue; it could indicate some type of inflammatory response. Alternatively, the overlap between lipid and A β may relate to an active role for lipid in plaque formation and possibly in dissolution, as has been proposed by other groups (Florent-Bechard et al., 2009; Hartmann et al., 2007; Martins et al., 2008). Interpretation of this discovery must await the completion of additional longer term animal studies and is beyond the scope of this paper. Most importantly, in these high definition IRENI images we can now clearly distinguish between plaque core, lipid halo and adjacent tissue. Moreover, while the lipid content is much higher in the halo, for the first time a small amount of the lipid can be detected even in the dense plaque core.

Subcellular features of mouse retina

The size of retinal neurons varies with function and location around the retinal wall. The three major types of neurons in the retina (photoreceptors, bipolar cells and ganglions) occupy layered positions spanning the retina from pigment epithelium to inner limiting membrane (Cuthbertson and Mandel, 1986). In nocturnal animals, such as rodents, photoreceptor cells are rod-dominated, with few cones.

Rod cells are excellent targets for subcellular analysis, as they are highly compartmentalized: the long outer segment consists mainly of flat disks rich in polyunsaturated fatty acids (PUFA), including some very long chain (C24 to C36) fatty acids (Suh et al., 2002) and rhodopsin, followed by a short inner segment containing mitochondria and Golgi apparatus, an inner nuclear segment containing the photoreceptor cell nucleus and a short tail embodying the synapses. Cells found within the second synaptic retinal layer include bipolar cells, amacrine cells and horizontal cells. Axons of photoreceptors form synapses with dendrites of bipolar cells, while amacrine and horizontal cells play regulatory roles and control some lateral processes. The complex network of bipolar and amacrine cells transfers information to the third layer of neurons of the visual pathway, the ganglion cells, whose long axons extend into the optic nerve.

IRENI images of eye tissue from a wild type mouse are shown in Fig. 4. A photomicrograph of the region imaged with the IRENI system (Fig. 4A). The five adjacent mosaic images, each 2×10 tiles, have been processed for the lipid peak at 2850 cm^{-1} to reveal the multiple layers (Fig. 4B). Spectra representative of the distinct biochemical signatures discovered are shown in Fig. 4C. The spectra, labeled a–i, are taken from corresponding locations in Fig. 4B, and scaled to give same peak height for the protein amide I band. In FTIR spectra, the lipid carbonyl (1738 cm^{-1}) corresponds to all fatty acid esters, and

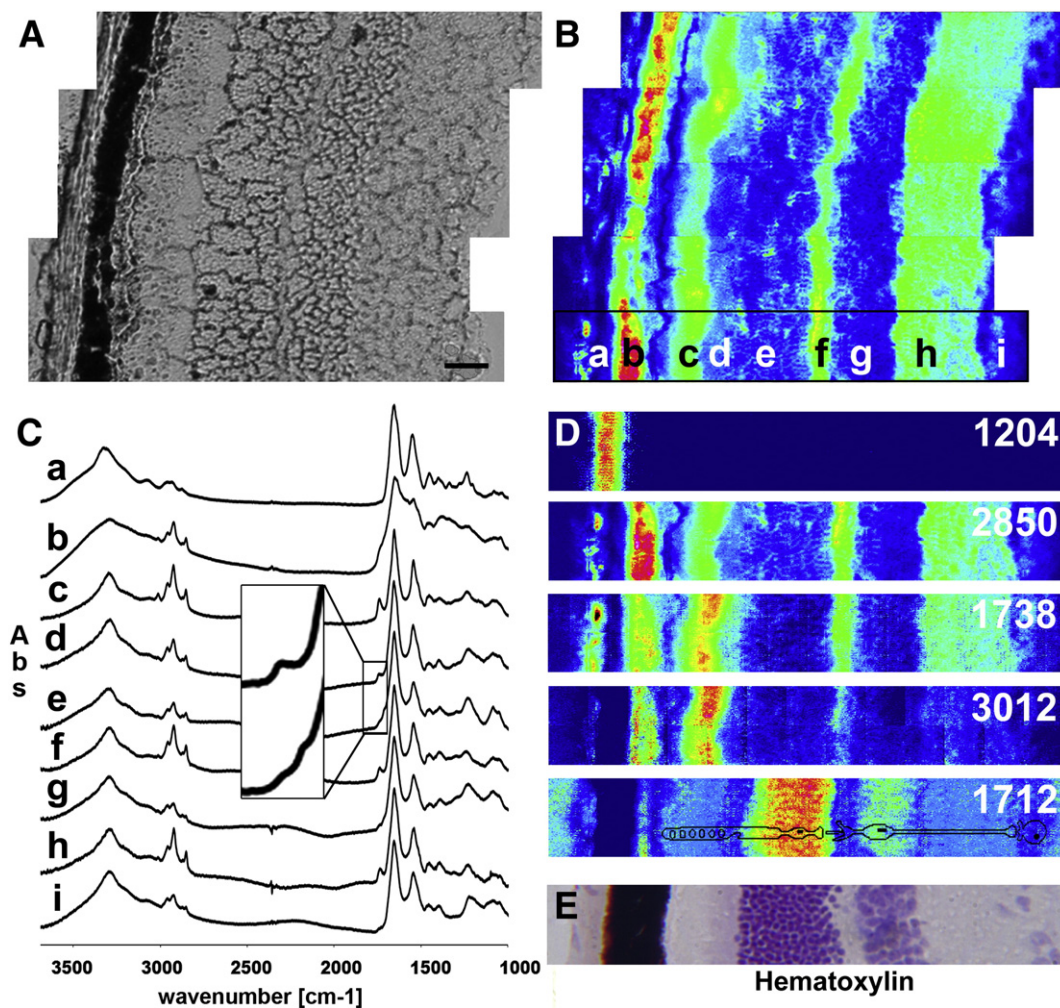


Fig. 4. FTIR images of retina tissue from a C57BL/6 mouse show sub-cellular details of photoreceptor system. A) Photomicrograph of retina. B) Five IRENI mosaics, 2×10 or 2×11 tiles (each tile = 64×64 pixels), processed on 2850 cm^{-1} to show lipid distribution. C) Spectra selected from retinal layers, identified by lowercase letters in (B), normalized to amide I peak height at 1655 cm^{-1} . D) Images from bottom mosaic (black box in (B)), with univariate processing for five characteristic peaks. Colors indicate component gradient from low (blue) to high (red), based on integrated band areas: 1204 cm^{-1} , 0.2–0.6; 2850 cm^{-1} , 0–0.9; 1738 cm^{-1} , 0.15–1.15; 3012 cm^{-1} , 0.0–0.45; 1712 cm^{-1} , 0.0–0.26. Bottom image has been overlaid with sketch of retinal neurons. E) Photomicrograph of serial section stained with hematoxylin. Scale bar $30 \mu\text{m}$.

is a proxy for lipid bilayer membranes. The peak at 3012 cm^{-1} corresponds to PUFA; the peak at 2850 cm^{-1} indicates the presence of saturated fatty acid (satFA), but includes contributions from the saturated portions of PUFA chains. The peak at 1712 cm^{-1} is ascribed to DNA and should be associated only with nuclei. Simple univariate processing for a few characteristic biomarker peaks (Fig. 4D) hints at the potential of IRENI for unparalleled multi-chemical imaging from a single data block. In Fig. 4D, bottom, a sketched outline of the three types of neurons (photoreceptor, bipolar and ganglion) is overlaid on an enlarged photomicrograph of tissue from a single 2×10 mosaic (Fig. 4B, delineated with a black box). A serial section, stained with hematoxylin, is shown below the processed IRENI images (Fig. 4E).

The choroid, the outermost layer of the tissue sample and external to the retina, is composed mainly of collagen fibrils, with a few cells; pigment epithelial cells line the inner layer and mesh with the end of the rod cells. The spectrum from choroid (Fig. 4C, a) displays the expected FTIR profile for collagen, and the IRENI image processed for a collagen peak (Fig. 4D, 1204 cm^{-1}) clearly shows the location of the choroid. A spectrum from the pigment epithelium (Fig. 4C, b) shows a fairly typical cellular profile of mixed protein and lipid in the CH stretch region. In the case of dense, uneven tissue, infrared light may be scattered (Bassan et al., 2010), with the result that there are undulations in the spectrum baseline. There is no scatter and a flat baseline in the non-absorbing region from 2700 to 1750 cm^{-1} , showing that the tissue quality is good. The fingerprint region (1800 – 900 cm^{-1}) contains intense broad bands, possibly due to pigment molecules, that confound further analysis at present. The CH stretch shows greater lipid content than would be seen in cell bodies; PUFA and satFA peaks could indicate the presence of compounds such as docosahexaenoic acid (DHA) that are stored here. *In vivo*, the epithelium is attached to photoreceptor cells but the retina appears to have become detached in some places. The photomicrograph shows a clear pale line between epithelium and photoreceptor layer that is matched by near-zero absorbance in the FTIR data (spectra not shown). In the IRENI images (Fig. 4D), a fine deep blue (low signal) line is seen, regardless of the band being processed.

Cone cells comprise only about 3% of the photoreceptor cells in the C57BL/J mouse (Carter-Dawson and Lavail, 1979), and probably exhibit a very similar spectral profile to rods. A spectrum from the rod outer segments (Fig. 4C, c) and the processed image (Fig. 4D, 1738 , 3012 and 2850 cm^{-1}) shows that fatty acid esters, especially PUFA, are concentrated here, as is expected for the PUFA-rich disks that also contain opsins, retinals and related visual proteins. We note that the minor baseline undulations seen in this and other spectra (Fig. 4C c–i) may be indicative of scatter, but do not present a problem for analysis. The spectrum from the rod inner segment (Fig. 4C, d) shows considerably less PUFA than the outer segment. Organelles such as mitochondria and Golgi apparatus are located in this portion of the rod cell. The FTIR spectrum from the photoreceptor nucleus layer (Fig. 4C, e) shows low lipid content (weak CH_2 stretch at 2850 and lipid carbonyl at 1738). The 1700 – 1800 region from spectra d and e has been enlarged to show peak characteristic for nucleic acids at 1712 cm^{-1} , in spectrum e, as well as phosphate bands at 1235 cm^{-1} and 1080 cm^{-1} . The IRENI image processed on the nucleic acid marker at 1712 cm^{-1} (Fig. 4D) is particularly strong in this layer, owing to the numerous nuclei that are scattered irregularly, but densely, throughout this layer. Densely-packed photoreceptor nuclei appear as dark purple-blue in the hematoxylin-stained section (Fig. 4E). This section was not immediately adjacent to the section imaged, and the width of the nuclear bodies is not an exact match, but suffices to confirm the assignment.

The spectrum from the outer plexiform layer (Fig. 4C, f) shows that it is rich in lipid (Fig. 4D, 2850 cm^{-1} , 1738 cm^{-1}) from the network of axons and synapses that enable communication between cells. The PUFA content is much lower than in the rod outer segment, confirming

that the PUFA are concentrated primarily in the rod disks. The spectrum of the bipolar cell nuclear layer (Fig. 4C, g) displays very low satFA and PUFA content (Fig. 4D, 2850 cm^{-1} , 1738 cm^{-1} , 3012 cm^{-1}), as seen for all cell bodies. The peak assigned to nucleic acids (Fig. 4D, 1712 cm^{-1}) is present, but its intensity is lower than in the outer nuclear layer, corresponding to a lower density of nuclei, as confirmed from the hematoxylin stain. The inner plexiform layer spectrum (Fig. 4C, h) is very similar to that of the outer plexiform layer, as might be expected, both layers showing up comparably in the IRENI images processed on the 2850 cm^{-1} and 1738 cm^{-1} peaks (Fig. 4D). The FTIR spectrum of a ganglion cell (Fig. 4C, i) is similar to the spectra of two other types of retinal neuron bodies. Individual retinal ganglion cells are dispersed close to the edge of the imaged tissue. They do not form a large distinctive nuclear layer (Fig. 4D, 1712 cm^{-1}).

FTIR maps of a rat retina were reported by Levine et al. (1999). Masks of $10 \times 30\text{ }\mu\text{m}^2$ to $10 \times 60\text{ }\mu\text{m}^2$ were used to achieve the separation of layers; hence, spectra attributed to the different layers represent averages with moderate spatial definition. The spectra showed a slight variation in satFA and PUFA, but the spatial resolution was insufficient to illustrate the complexity revealed by IRENI. The phospholipid composition of retinal disk membranes in the rod outer segment is directly related to optimal visual function (Jeffrey et al., 2001). Composition can be altered by changes in dietary PUFA (Fliesler and Anderson, 1983; Schnebelen et al., 2009; Suh et al., 2002); increased dietary PUFA has been connected to improved repair following injury and to elevation of neuroprotective metabolites (Connor et al., 2007). The role of biochemical composition of retina has been shown in relation to the age-related macular degeneration, retinopathy, and vitamin deficiency (Simopoulos and Bazan, 2009). IRENI offers tremendous potential for the study of biochemical composition of retina in many models of health, disease, and dietary modification. In future work, we will examine *in vivo* imaging of live cells with this system.

Conclusions

IRENI makes it possible to study biochemical changes within single cells and to characterize their surroundings; it should find wide application as a tool for research in neuroscience. IRENI yields true diffraction-limited chemical images at all mid-IR wavelengths. The use of 12 bright synchrotron beams for illumination makes it possible to rapidly image a sample area of $50 \times 50\text{ }\mu\text{m}^2$, maintaining a high signal-to-noise ratio with extremely short acquisition times, usually a matter of a few minutes. The dimensions of cells in the CNS are much greater than the pixel sampling of IRENI ($0.54 \times 0.54\text{ }\mu\text{m}^2$), enabling subcellular FTIR imaging with the highest currently achievable spatial resolution. We have shown individual CA1 neurons in the hippocampus of a 3xTg mouse, and neurons located in the proximity of an amyloid plaque in a TgCRND8 mouse. We have also demonstrated that in a mouse model of AD, neuritic amyloid plaques are infiltrated with lipid, while the aggregated A β peptide extends into the surrounding halo of lipid. These results are important, because the role of lipids has not been fully characterized; it may be an important molecular component of the inflammatory response in AD and may also participate in plaque formation and dissolution. Images of retina sections reveal much greater variation in the natural biochemical signatures of neuronal layers than was previously thought to exist. Label-free imaging of subcellular organization is now possible through the spectrochemical specificity of FTIR and the spatial resolution of IRENI.

Acknowledgments

The authors thank Dr. David Westaway, Dr. Robert Julian, Prof. Jason Morrison and Dr. Igor Tretiakov for advice and technical assistance. This work was supported by grants from the Canadian Institutes of Health Research, the Manitoba Health Research Council,

and NSERC. Dr. Benedict Albeni holds The Honourable Douglas Everett, Patricia Everett and the Royal Canadian Properties Endowment Fund Chair and is a Research Affiliate at the Centre on Aging, University of Manitoba. Dr. Del Bigio holds the Canada Research Chair in Developmental Neuropathology. The IRENI project is supported by NSF Grant Nos. DMR-0619759. The SRC is operated under NSF Grant No. DMR-0537588.

References

- Bassan, P., Kohler, A., Martens, H., Lee, J., Byrne, H.J., Dumas, P., Gazi, E., Brown, M., Clarke, N., Gardner, P., 2010. Resonant Mie Scattering (RMieS) correction of infrared spectra from highly scattering biological samples. *Analyst* 135, 268–277.
- Carr, G.L., 2001. Resolution limits for infrared microspectroscopy explored with synchrotron radiation. *Rev. Sci. Instrum.* 72, 1613–1619.
- Carter-Dawson, L.D., Lavail, M.M., 1979. Rods and cones in the mouse retina. I. Structural analysis using light and electron microscopy. *J. Comp. Neur.* 188, 245–262.
- Chalmers, J.M., Griffiths, P.R., 2002. *Handbook of Vibrational Spectroscopy*, vol. 1–5. Wiley, Chichester UK.
- Chishti, M.A., Yang, D., Janus, C., Phinney, A.L., Horne, P., Pearson, J., Strome, R., Zuker, N., Loukides, J., French, J., Turner, S., Lozza, G., Grilli, M., Kunicki, S., Morrisette, C., Paquette, J., Gervais, F., Bergeron, C., Fraser, P.E.M., Carlson, G.A., St. George-Hyslop, P., Westaway, D., 2001. Early-onset amyloid deposition and cognitive deficits in transgenic mice expressing a double mutant form of amyloid precursor protein 695. *J. Biol. Chem.* 276, 21562–21570.
- Connor, K., SanGiovanni, J., Lofgvis, C., Aderman, C.M., Chen, J., Higuchi, A., Hong, S., Pravda, E.A., Majchrzak, S., Carper, D., Hellstrom, A., Kang, J.X., Chew, E.Y., Salem Jr., N., Serhan, C.N., Smith, L.E.H., 2007. Increased dietary intake of ω -3 polyunsaturated fatty acids reduced pathological retinal angiogenesis. *Nat. Med.* 13, 868–873.
- Cuthbertson, R.A., Mandel, T.E., 1986. Anatomy of the mouse retina. Endothelial cell-pericyte ratio and capillary distribution. *Invest Ophthalmol. Visual Sci.* 27, 1659–1664.
- Dumas, P., Sockalingum, G.D., Sule-Suso, J., 2007. Adding synchrotron radiation to infrared microspectroscopy: what's new in biomedical applications? *Trends Biotechnol.* 25, 40–44.
- Fliesler, S.J., Anderson, R.E., 1983. Chemistry and metabolism of lipids in the vertebrate retina. *Prog. Lipids Res.* 22, 79–131.
- Florent-Bechard, S., Desbene, C., Garcia, P., Allouche, A., Youssef, I., Escanye, M.C., Koziel, V., Hanse, M., Malaplate-Armand, C., Stenger, C., Kriem, B., Yen-Potin, F.T., Olivier, J.L., Pillot, T., Oster, T., 2009. The essential role of lipids in Alzheimer's disease. *Biochimie* 91, 804–809.
- Gambis, A., Dourlen, P., Steller, H., Bertrand, Mollereau, 2011. Two-color in vivo imaging of photoreceptor apoptosis and development in *Drosophila*. *Develop. Biol.* 351, 128–134.
- Guo, L., Duggan, J., Cordeiro, M.F., 2010. Alzheimer's disease and retinal neurodegeneration. *Curr. Alzheimer Res.* 7, 3–14.
- Hartmann, J., Kiewert, C., Duysen, E.G., Lockridge, O., Greig, N.H., Klein, J., 2007. Excessive hippocampal acetylcholine levels in acetylcholinesterase-deficient mice are moderated by butyrylcholinesterase activity. *J. Neurochem.* 100, 1421–1429.
- Huffman, S.W., Bhargava, R., Levin, I.W., 2002. Generalized implementation of rapid-scan Fourier transform infrared spectroscopic imaging. *Appl. Spectrosc.* 56, 965–969.
- Jeffrey, B.G., Weisinger, H.S., Neuringer, M., Mitchell, D.C., 2001. The Role of Docosahexaenoic Acid in Retinal Function. *Lipids* 36, 859–870.
- Jensen, T.H., Bech, M., Bunk, O., Menzel, A., Bouchet, A., Le Duc, G., Feidenhans'l, R., Pfeiffer, F., 2011. Molecular X-ray computed tomography of myelin in a rat brain. *Neuroimage* 57, 124–129.
- Kastyak, M.Z., Szczerbowska-Boruchowska, M., Adamek, D., Tomik, B., Lankosz, M., Gough, K.M., 2010. Pigmented creatine deposits in Amyotrophic Lateral Sclerosis central nervous system tissues identified by Synchrotron FTIR microspectroscopy and X-ray fluorescence spectromicroscopy. *Neuroscience* 166, 1119–1128.
- Kokotas, H., Grigoriadou, M., Petersen, M.B., 2011. Age-related macular degeneration: genetic and clinical findings. *Clin. Chem. Lab. Med.: CCLM/FESCC* 49, 601–616.
- Kuzyk, A., Kastyak, M.Z., Agrawal, V., Gallant, M., Sivakumar, G., Rak, M., Del Bigio, M.R., Westaway, D., Julian, R., Gough, K.M., 2010. Association among amyloid plaque, lipid, and creatine in hippocampus of TgCRND8 mouse model for Alzheimer disease. *J. Biol. Chem.* 285, 31202–31207.
- Levine, S.M., Radel, J.D., Sweat, J.A., Wetzel, D.L., 1999. Microchemical analysis of retina layers in pigmented and albino rats by Fourier transform infrared microspectroscopy. *Biochem. Biophys. Acta* 1473, 409–417.
- Lucas, S., Rothwell, N.J., Gibson, R.M., 2006. The role of inflammation in CNS injury and disease. *Br. J. Pharmacol.* 147 (S1), S232–S240.
- Martins, I.C., Kuperstein, I., Wilkinson, H., Maes, E., Vanbrabant, M., Jonckheere, W., Van Gelder, P., Hartmann, D., D'Hooge, R., De Strooper, B., Schymkowitz, J., Rousseau, F., 2008. Lipids revert inert A β amyloid fibrils to neurotoxic protofibrils that affect learning in mice. *EMBO J.* 27, 224–233.
- Mattson, M.P., 2004. Pathways towards and away from Alzheimer's disease. *Nature* 430, 631–639.
- Miller, L.R., Smith, R.J., 2005. Synchrotrons versus Globars, point-detectors versus focal plane arrays: selecting the best source and detector for specific infrared microspectroscopy and imaging applications. *Vib. Spectrosc.* 38, 237–240.
- Nasse, M.J., Walsh, M.J., Mattson, E.C., Reininger, R., Kajdacsy-Balla, A., Macias, V., Bhargava, R., Hirschmugl, C.J., 2011. High-resolution Fourier-transform infrared chemical imaging with multiple synchrotron beams. *Nature Meth.* 8, 413–416.
- Nasse, M.J., Reininger, R., Kubala, T., Janowski, S., Hirschmugl, C., 2007. Synchrotron infrared microspectroscopy imaging using a multi-element detector (IRMSI-MED) for diffraction-limited chemical imaging. *Nucl. Instrum. Methods Phys. Res., Sect. A* 582, 107–110.
- Oddo, S., Caccamo, A., Shepherd, J.D., et al., 2003. Triple-transgenic model of Alzheimer's disease with plaques and tangles: intracellular A β and synaptic dysfunction. *Neuron* 39, 409–421.
- Rak, M., Del Bigio, M.R., Mai, S., Westaway, D., Gough, K.M., 2007. Dense-core and diffuse Abeta plaques in TgCRND8 mice studied with synchrotron FTIR microspectroscopy. *Biopolymers* 87, 207–211.
- Schjeide, B.M., McQueen, M.B., Mullin, K., Divito, J., Hogan, M.F., Parkinson, M., Hooli, B., Lange, C., Blacker, D., Tanzi, R.E., Bertram, L., 2009. Assessment of Alzheimer's disease case-control associations using family-based methods. *Neurogenetics* 10, 19–25.
- Schnebelen, C., Gregoire, S., Pasquis, B., Joffre, C., Creuzot-Garcher, C.P., Bron, A.M., Bretilon, L., Acar, N., 2009. Dietary n-3 and n-6 PUFA enhance DHA incorporation in retinal phospholipids without affecting PGE1 and PGE2 levels. *Lipids* 44, 465–470.
- Schulz, G., Weitkamp, T., Zanette, I., Pfeiffer, F., Beckmann, F., David, C., Rutishauser, S., Reznikova, E., Müller, B., 2010. High-resolution tomographic imaging of a human cerebellum: comparison of absorption and grating-based phase contrast. *J. R. Soc. Interface* 7, 1665–1676.
- Selkoe, D.J., 2004. Cell biology of protein misfolding: the examples of Alzheimer's and Parkinson's diseases. *Nature Cell Biol.* 6, 1054–1061.
- Seshadri, S., Khurana, R., Fink, A.L., 1999. Fourier transform infrared spectroscopy in analysis of protein deposits. *Methods Enzymol.* 309, 559–576.
- Simopoulos, A.P., Bazan, N.G., 2009. Omega-3 fatty acids, the brain and retina. *World Rev. Nutr. Diet.* vol. 99.
- Suh, M., Wierzbicki, A.A., Clandinin, M.T., 2002. Dietary n-3 FA modulate long and very long chain FA content, rhodopsin content and rhodopsin phosphorylation in rat rod outer segment after light exposure. *Lipids* 37, 253–260.
- Wiens, R., Rak, M., Cox, N., Abraham, S., Juurlink, B.H.J., Kulyk, W.M., Gough, K.M., 2007. Synchrotron FTIR microspectroscopic analysis of the effects of anti-inflammatory therapeutics on wound healing in laminectomized rats. *Anal. Bioanal. Chem.* 387, 1679–1689.
- Winton, M.J., Lee, E.B., Sun, E., Wong, M.M., Leight, S., Zhang, B., Trojanowski, J.Q., Lee, V.M.-Y., 2011. Intraneuronal APP, not free A β peptides in 3xTg-AD mice: implications for tau versus A β -mediated Alzheimer neurodegeneration. *J. Neurosci.* 31, 7691–7699.
- Witte, S., Negrean, A., Lodder, J.C., de Kock, C.P.J., Silva, G.T., Mansvelter, H.D., Groot, M.L., 2011. Label-free live brain imaging and targeted patching with third-harmonic generation microscopy. *PNAS* Mar. 28, 1–6.
- MATLAB® (2009, The MathWorks, Natick, MA); Felix Totir and Ian Howat (2010) ENVI file reader/writer, available from: <http://www.mathworks.com/matlabcentral/fileexchange/27172>.